ACCEPTED VERSION

Stephan Kruse, Jingjing Ye, Zhiwei Sun, Antonio Attili, Bassam Dally, Paul Medwell, Heinz Pitsch
Experimental investigation of soot evolution in a turbulent non-premixed prevaporized toluene flame

Final publication at http://dx.doi.org/10.1016/j.proci.2018.05.075

PERMISSIONS

https://www.elsevier.com/about/our-business/policies/sharing

Accepted Manuscript

Authors can share their accepted manuscript:

Immediately

- via their non-commercial personal homepage or blog
- by updating a preprint in arXiv or RePEc with the accepted manuscript
- via their research institute or institutional repository for internal institutional uses or as part of an invitation-only research collaboration work-group
- directly by providing copies to their students or to research collaborators for their personal use
- for private scholarly sharing as part of an invitation-only work group on commercial sites with which Elsevier has an agreement

After the embargo period

- via non-commercial hosting platforms such as their institutional repository
- via commercial sites with which Elsevier has an agreement

In all cases accepted manuscripts should:

- link to the formal publication via its DOI
- bear a CC-BY-NC-ND license – this is easy to do
- if aggregated with other manuscripts, for example in a repository or other site, be shared in alignment with our hosting policy
- not be added to or enhanced in any way to appear more like, or to substitute for, the published journal article

23 March 2021

---

http://hdl.handle.net/2440/118343

Experimental investigation of soot evolution in a turbulent non-premixed prevaporized toluene flame

Stephan Kruse[a,*], Jingjing Ye[b], Zhiwei Sun[b], Antonio Attili[a], Bassam Dally[b], Paul Medwell[b], Heinz Pitsch[a]

[a]*Institute for Combustion Technology - RWTH Aachen University, Templergraben 64, Aachen 52062, Germany*
[b]*School of Mechanical Engineering - The University of Adelaide, S.A. 5005, Australia*

Abstract

The formation, growth, and oxidation of soot in turbulent prevaporised toluene diffusion flames stabilized on a jet-in-hot-coflow (JHC) burner are investigated in this study. Flame structure, local gas temperature as well as local soot volume fraction and primary soot particle diameter, are simultaneously detected by means of OH planar laser-induced fluorescence (PLIF), non-linear two-line atomic fluorescence (nTLAF) of indium, and time resolved (TiRe) laser-induced incandescence (LII), respectively. The collected data sets were used to generate joint statistics of soot properties and flame characteristics and provided new insights into the turbulent soot–flame interaction. In particular, the interaction of OH and soot as a driving mechanism for soot oxidation is of particular interest as it has been proven to be challenging to numerical models. Statistics of soot volume fraction and primary particle size in the OH layer reveal quantitative information on the soot oxidation process. Mean soot volume fraction and primary soot particle size conditioned on temperature and OH signal intensity indicate that, due to preferential diffusion of soot, high soot volume fraction and primary soot particle diameter of up to 50 nm are present at low temperatures and low OH concentration. In the soot oxidation region, statistical analysis of the soot parameters disclose that clusters of high soot volume fraction mostly consist of large primary particles. Observations from instantaneous images and the presence of large primary particles inside the OH layer suggest that the oxidation is not sufficiently fast to burn the soot completely.

Keywords:
Soot in turbulent flames, soot oxidation, temperature, soot particle diameter, soot volume fraction

*Corresponding author: s.kruse@itv.rwth-aachen.de
Email address: s.kruse@itv.rwth-aachen.de (Stephan Kruse)

1. Introduction

Soot formation is an undesirable process in many practical combustion devices, such as diesel engines, and direct injection gasoline engines, and gas turbines. Soot originates from fuel pyrolysis or combustion under rich conditions. It is well-known to have tremendous negative impacts on the environment and on human health [1, 2]. Moreover, soot emission is an indicator of incomplete, and thus inefficient combustion [3]. Hence, a better understanding of the formation, growth, and oxidation of soot is required in order to optimize the combustion efficiency and meet increasingly stringent emission standards.

Most detailed experimental and numerical studies on soot have been performed in various laminar flame configuration yielding fundamental knowledge of the complex soot formation and its oxidation under well-defined conditions [4]. Although soot formation in turbulent flames is more relevant for practical combustion devices, only a limited number of studies have investigated the soot formation in turbulent flames. The strong interaction and highly non-linear correlation of soot formation, turbulence and chemistry require spatially and temporally well-resolved simulations or experiments that simultaneously yield multiple quantities. Therefore, both simulation and experiment become extremely complex and costly.

Comprehensive datasets of two and three dimensional turbulent n-heptane flames have been obtained from direct numerical simulations (DNS) including chemistry of soot precursors and a higher-order statistical soot model [5, 6]. These studies reveal high sensitivity of soot precursor concentration to the local dissipation rate, thereby highlighting the significant importance of the mixing field on the soot formation. In further studies, Attili et al. [7] observed the presence of soot at small mixture fractions (Z) below the stoichiometric mixture fraction (Z_{st}). It was demonstrated that these soot patches emerge through areas of local flame extinction, whereas soot crossing the burning OH layer was not obtained [7].

Recent advancement of laser diagnostics has enabled the simultaneous detection of soot and flame parameters with high spatial and temporal resolution. Park et al. [8] presented joint statistics of Z and f_v in the soot inception region by using a combined setup of laser-induced incandescence (LII), particle image velocimetry (PIV), and krypton laser-induced fluorescence (Kr-LIF). Their observations revealed that the peak soot volume fraction in the soot inception region occurs in the mixture fraction range of $Z = 0.3$–0.4, where the concentration of

soot precursors is the highest [8].

Detailed experiments under well-defined conditions of a turbulent sooting ethylene flame have been provided by Köhler et al. [9, 10]. Data of the flow field, gas temperature (T), f_v, OH as well as polycyclic aromatic hydrocarbon (PAH) distribution and local Z were obtained by means of laser diagnostics [9, 10]. Gu et al. [11] have recently extended this comprehensive data set by simultaneous measurements of f_v, primary particle size (d_p), number density (N_p), and T. Strong correlations were found for f_v, d_p, and number density (N_p), whereas these soot parameters exhibit moderate correlation with T. However, the interaction of soot and OH layers, which is particularly relevant for soot oxidation, has not been analyzed in these studies. Lee at al. [12] investigated the interaction of soot and OH in turbulent ethylene flames. It was found that the spatial overlap of soot and OH causes a reduction of f_v [12]. Independent of the fuel, the same phenomenon has also been reported in turbulent methane flames by Franzelli et al. [13].

Although the strong interaction of soot and reaction surface, and its relevance for soot oxidation, have been reported for different fuels [12, 13], quantitative analysis of the soot parameters (f_v and d_p) within the reaction zone is absent. Therefore, this study aims to quantitatively analyze the soot–flame interaction in a turbulent flame. Prevaporized toluene has been used as it is a simple aromatic compound and is a common component of diesel and gasoline surrogates [14, 15]. While toluene has been frequently studied in laminar flames as a blending component where its dominate role on soot and PAH formation has been reveleaad, soot measurements in turbulent toluene flames are absent. [16, 17].

Simultaneous laser diagnostics were performed to detect OH, T, f_v, and d_p. Conditional data and joint statistics is presented to provide quantitative information on the soot-flame interaction

2. Experimental setup

2.1. Burner configuration

The current burner setup is a modification of the well-established jet-in-hot-coflow burner (JHC) [18, 19]. The fuel is introduced through a central insulated pipe with an inner diameter of 4.6 mm and a tapered end at the exit. The length-to-diameter ratio of the fuel jet is more than 100 to ensure fully developed turbulent pipe flow at the exit. The fuel jet was surrounded by a coflow of gases produced by a lean, laminar nitrogen (N_2)-diluted natural gas/air flame stabilized on a porous bed. The annular porous-bed burner with an inner diameter of 108

mm was located 25 mm upstream of the jet exit to minimize heat transfer to the central fuel jet while ensuring for a homogeneous coflow composition at the jet exit. An annular shielding flow of room air was issued from a 22 mm wide ring around the hot coflow.

The exit velocity of the shielding air flow was 0.4 m/s. The flow rates of natural gas, air, and N_2 were set by mass flow controllers to achieve oxygen mass fraction Y_{O_2} = 0.083 and a temperature T = 1544 K in the hot coflow stream with an exit velocity of 0.8 m/s. The fuel stream was a mixture of prevaporized toluene and N_2 as a carrier gas. The toluene mass fraction (Y_F) was kept at 0.25 and the Reynolds number at the fuel jet exit was 10000.

Toluene was vaporized and mixed with the carrier gas in a controlled evaporator and mixer unit (CEM, Bronkhorst). After the CEM unit, the gas mixture was delivered to the burner via heated tubes. The temperature in the CEM and the tubes was maintained at 453 K to prevent fuel condensation.

2.2. Optical arrangement

Time-resolved (TiRe)-LII, OH planar laser-induced fluorescence (LIF), and non-linear two atomic fluorescence (nTLAF) are employed to simultaneously detect OH, T, f_v, and d_p. A schematic of the optical system is presented in Fig. 1.
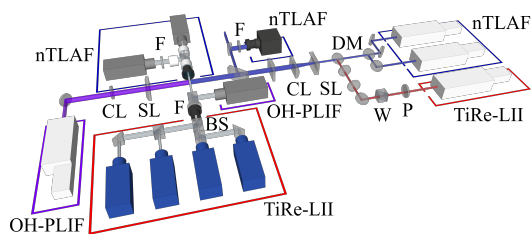

Figure 1: Optical setup for simultaneous detection of temperature (nT-LAF) and d_p as well as f_v (TiRe-LII). DM, dichroic mirror; W, waveplate; P, polarizer; CL, cylindrical lens; SL, spherical lens; F, bandpass filter

The combined TiRe-LII and nTLAF setup was used in previous studies [11, 20]. The optical system has been extended by the OH-PLIF diagnostic in the current study. The imaging sequence started with the nT-LAF followed by the OH-PLIF and TiRe-LII with 1 μs and 3 μs delay, respectively, to avoid signal interference between the various systems.

The nTLAF of indium is used to determine the local gas temperature [21]. A laser ablation technique was used to seed indium nanoparticles to the fuel stream [22]. Two dye lasers (Quantel, TDL 90) pumped

by Nd:YAG lasers (Quantel, BrilliantB and YG-980) generated the Stokes and anti-Stokes beams to excite the indium. Both beams were formed into light sheets with a height of 16 mm and a thickness of 0.25 mm, focused on the jet centerline. In order to avoid interference, the anti-Stokes beam was emitted 120 ns after the Stokes beam. The corresponding signals were collected by a Nikon camera lens (f/1.2). Behind the lens, the incoming light was split by a dichroic mirror. The Stokes and anti-Stokes nTLAF signals were collected by intensified CCD (ICCD) cameras (Princeton Instruments Pi-Max 4) equipped with custom-made narrow bandpass filters centered at 451.4 nm (FWHM = 1.32 nm) and 410.4 nm (FWHM = 1.08 nm), respectively [23]. The gating time of the cameras was set to 30 ns to suppress the background flame luminosity. To account for spatial and temporal fluctuations of the laser sheet, part of the light sheets was deflected to a quartz cuvette filled with a suspension of distilled water and titanium oxide nanoparticles. The Mie scattering from these nanoparticles was recorded by a CCD camera (MegaPuls II, ES 4020) to correct for vertical light sheet inhomogeneity on a shot-to-shot basis. The quantification of nTLAF was described in detail in [11]. Briefly, in order to obtain calibration factors, the nTLAF and thermocouple measurements were performed in the hot product stream of a well-characterized flat-flame burner on a daily basis. The uncertainties of single shot nTLAF temperature measurements in a turbulent flame have been previously reported to be in the range of ±120 K [11].

The fundamental (1064 nm) of a Nd:YAG laser (Quantel, BrilliantB) was used to heat up the soot particles for TiRe-LII measurements. The beam was formed to a collimated light sheet with 20 mm height and 0.25 mm width by a sheet optic. In order to avoid excessive sublimation of the soot particles, the laser fluence was set to approximately 0.3 mJ/cm^2. The radiation of the soot particles was collected by a Nikon f/1.4 camera lens equipped with a bandpass filter (435 nm, FWHM = 48.8 nm). Beam splitters behind the camera lens deflected the soot radiation to four ICCD camera heads (pco, HSFC Pro) to record the LII signal decay in a series of four consecutive images. The first image was instantaneously recorded with the laser pulse, the following three were detected with a delay of 80 ns, 160 ns, and 240 ns. The gating time of all four cameras was 40 ns. The prompt LII image yields the local soot volume fraction. The intensity ratios of the sequential images were compared to computed LII signal decay rates to extract the primary particle diameter. Detailed information on the LII model are provided in [24]. The modeling assumption of non-aggregated, mono-disperse soot

particles results in an overestimation of d_p by a factor of two [11]. The detection limit of the particle size is 5 nm [20], the uncertainty in d_p is 20% [11]. For f_v determination, LII calibration measurements were performed in a Santoro flame.

For qualitative OH-PLIF measurements, OH was excited on the line $Q_1(8)$ by a 283.58 nm laser beam generated in a dye laser (LambdaPhysics, ScanMate) pumped by the second harmonic of a Nd:YAG laser (Quantel, Brilliant B). The beam was formed to a light sheet and overlapped with the LII and nTLAF laser sheets. The OH-LIF signal was reflected by a dichroic mirror and imaged by a catadioptric f/1.2 UV camera lens equipped with a narrow bandpass filter (310 nm, FWHM = 10 nm) on an ICCD camera (Princeton Instruments, PI-MAX).

Spatial matching and calibration of all images were achieved by imaging a target in the light sheet plane. The resulting field of view had a height of 14 mm and the in–plane spatial resolution was determined to be 0.0887 mm/pixel. All images were corrected for vignetting, chip inhomogeneities and background flame luminosity.

3. Mean flame structure and soot distribution

The mean distributions of f_v, d_p, T, and OH averaged from 499 single images at various heights above the jet exit plane are shown in Fig. 2. As nTLAF is limited to $T \geq 800$ K, only data above 800 K are included in the calculation of the mean temperature. For nTLAF and TiRe-LII, the beam propagates from the left to the right side of the images (-20 mm $\leq x \leq$ 20 mm). The asymmetic soot distribution in the range of 60 mm $\leq$ $y \leq 210$ mm is a result of beam steering [25]. In order to minimize errors induced by beam steering, statistical data are obtained from the half of the image on the beam entrance side. The direction of the OH-PLIF beam is from right to left. The radial asymmetry of the OH-PLIF signal also occurs at height 60 mm $\leq x \leq 210$ mm and it is predominantly attributed to absorption of laser energy by soot and PAH.

The mean images of OH-PLIF and T indicate a thin, distinct flame structure slightly lifted from the fuel nozzle. At the outer radial locations up to $y \leq 80$mm, OH from the hot coflow is detected. Consistent with findings in [18], this observation reveals that the influence of the coflow diminishes at approximately $y = 80$ mm. Hereafter, the flame develops to a non-premixed air-fuel flame. Strong interference of OH-PLIF and nTLAF signal with PAH-LIF is observed at the jet centerline at a height of 40 mm $\leq y \leq 100$ mm.
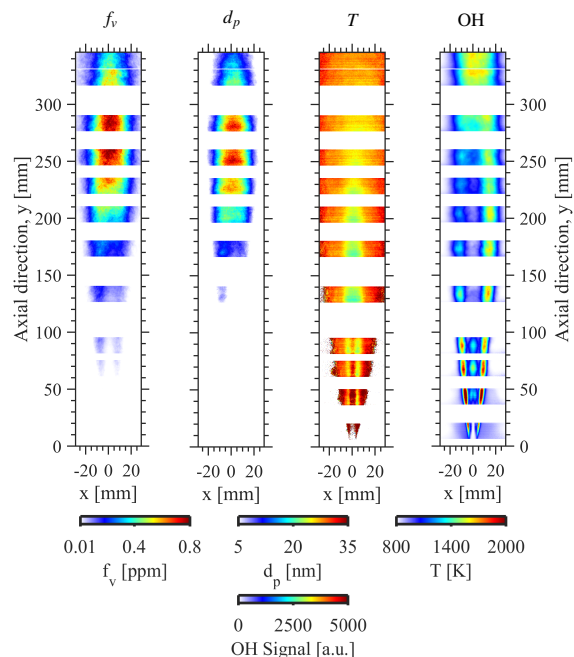

Figure 2: Averaged distribution of f_v, d_p, T, and OH at various heights above the burner.

The first measurable soot was detected at $y = 70$ mm. The mean images of f_v and d_p reveal the characteristic regions of soot formation (70 mm $\leq y \leq$ 170), soot transport by turbulence (195 $\leq y \leq$ 290 mm), and soot oxidation (320 mm $\leq y \leq$ 350 mm) that have been also reported previously [12, 13].

Upstream of $y = 130$ mm, d_p is below the detection limit of 5 nm. Further downstream, both f_v and d_p increase in the soot formation region. Meanwhile, a core of low temperature is apparent at the jet centerline. A comparison of f_v, d_p, T, and OH images indicates that the formation of soot is confined to a narrow layer on the fuel rich side of OH with elevated temperatures.

For $y \geq 195$ mm, the soot is transported by the turbulent flow field resulting in a wide radial distribution of soot. Within 245 mm $\leq y \leq$ 290 mm, f_v and d_p remain almost constant. The peaks of f_v and d_p are observed on the jet centerline and decrease with increasing distance from the centerline. In contrast, the temperature and OH signal are lowest on the jet centerline and increase towards the outer region.

In the range from $y = 315$ mm to 350 mm, the mean f_v and d_p are significantly reduced and the distribution is narrowed towards the centerline due to enhanced soot oxidation.

In order to provide further information on the flame structure, one-dimensional calculation are performed

in physical space with unity Lewis numbers using FlameMaster [26] and the kinetic mechanism presented in [14]. As shown by [27], imposing unity Lewis numbers is the most appropriate choice to capture the structure of turbulent non-premixed flames. The oxidizer is air and the fuel stream consists of an N_2–toluene mixture ($Y_F = 0.25$). According to [28], a characteristic strain rate is approximated based on the inverse of the global residence time to be 25 s^{-1}.

Figure 3 illustrates the profiles of T, dimer production rate as a measure for soot formation, naphthalene (A2) as a representative soot precursor, and OH mass fraction in the mixture fraction space. It is evident that soot precursors are present at $Z \geq Z_{st}$ with the maximum mass fraction at $Z = 0.4$ and temperatures of 1220 K $\leq T \leq$ 1600 K. The dimer production rate follows the same trend, whereas the peak rate is obtained at slightly higher Z. In contrast, OH is solely present in a narrow range at high temperatures and around Z_{st}. This characteristic makes OH a good marker of the flame region. The profiles indicate that OH and soot do not overlap. Additional flamelet computations, with different strain rates in the range expected in the turbulent flame, revealed that the flame structure observed in Fig. 3 is not affected (not shown).
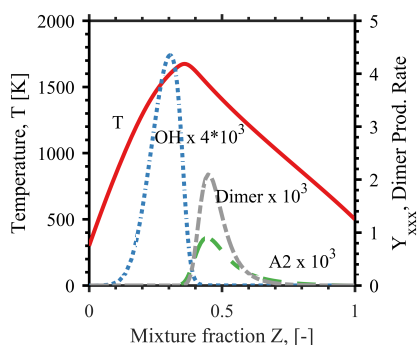

Figure 3: Profiles of T, Y_{OH}, Y_{A2}, and dimer production rate obtained from flamelet simulation. Fuel side: Y_F = 0.25 balanced with N_2, T_F = 500 K; Oxidizer side: Y_{O_2} = 0.233 balanced with N_2, T_{O_2} = 298 K. Strain rate is 25 s^{-1}

4. Statistical analysis of soot-OH interaction in turbulent flame

Previous experimental studies of turbulent sooting flames have qualitatively reported the spatial overlap of OH and soot [12, 13]. The simultaneous and quantitative detection of soot and flame characteristics enables a detailed analysis of soot parameters in the OH layer.

To illustrate the soot–OH interaction, Fig. 4 depicts instantaneous representative images of the f_v, d_p, and T from the soot formation, mixing-dominated, and oxidation zone. The iso-contours of two OH signal intensities are plotted as gray and black lines in the instantaneous images.

In the soot formation region (165 mm $\leq y \leq$ 180 mm), soot is concentrated in small segregated clusters. Regions without soot are particularly present in low-temperature regions around the jet centerline. The temperature increases towards the OH layer. Soot clusters with high f_v and d_p are found close to the OH layer on the fuel rich side, whereas soot is absent in the OH layer and on the lean side.

At 245 mm $\leq y \leq$ 260 mm, the local f_v and d_p are significantly higher compared to the formation zone. The soot patterns follow the flow and are stretched and wrapped by turbulent vortices resulting in wide distribution and high spatial gradients of f_v. Soot is also present in areas of lower temperatures. This is due to the very low diffusivity of soot particles compared to that of temperature. This differential diffusion promotes a significant transport of soot in the temperature space [6]. Although the soot is still predominately distributed in elongated structures in the rich side of the flame, discrete ligaments of soot are present in the OH layer and even on the lean side of the non-premixed flame.

At the highest axial position, the soot appears in confined regions with $f_v \geq$ 3 ppm and $d_p \geq$ 60 nm in the zone between the OH layers where the local temperature is low. Similar to observations in the mixing dominated area, soot patterns with high d_p penetrate the OH layer. The soot is mostly oxidized in the OH layer, nevertheless, small soot clusters are found on the lean side of the OH layer.

The presence of soot in the OH layer is assessed by joint probability density functions (jpdf) of f_v and OH signal intensity as well as d_p and OH signal intensity presented in Fig. 5. The mean of f_v and d_p conditioned on OH are also included in the plots. The samples are obtained from 499 single images and are spatially averaged over 0.45 mm × 0.45 mm.

Figure 5 shows that, in the formation region, soot is present at locations where the OH signal is in the range of background noise, whereas soot is absent at high OH signal intensities. This finding is consistent with the mean images and the flamelet simulation in Fig. 3. The conditional means of f_v and of d_p reveal that, soot in this region is still formed of primary particle of rather small size. With increasing axial distance, f_v and d_p increase remarkably. This is consistent with an increase of the volume fraction and mass of soot mostly related to the
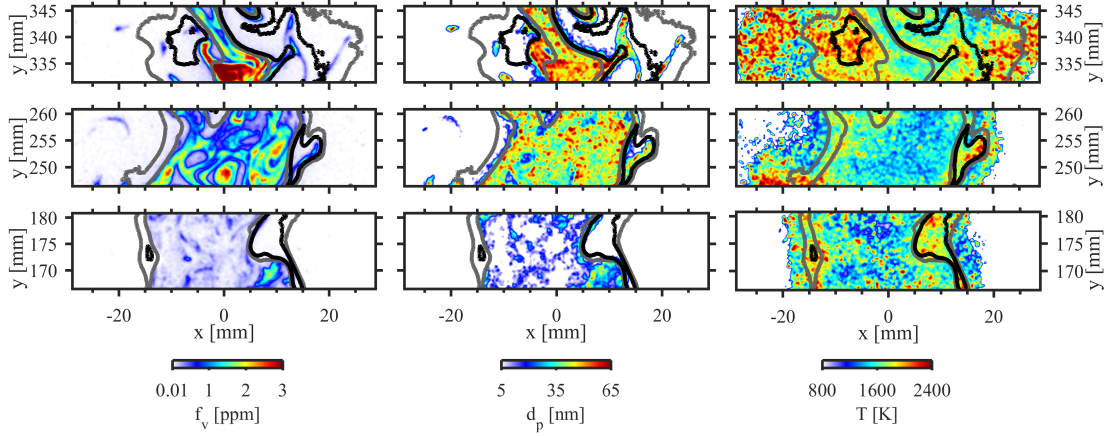
Figure 4: Instantaneous images of f_v, d_p, and T overlaid with OH iso-contours (2000 counts: gray line, 5000 counts: black line)
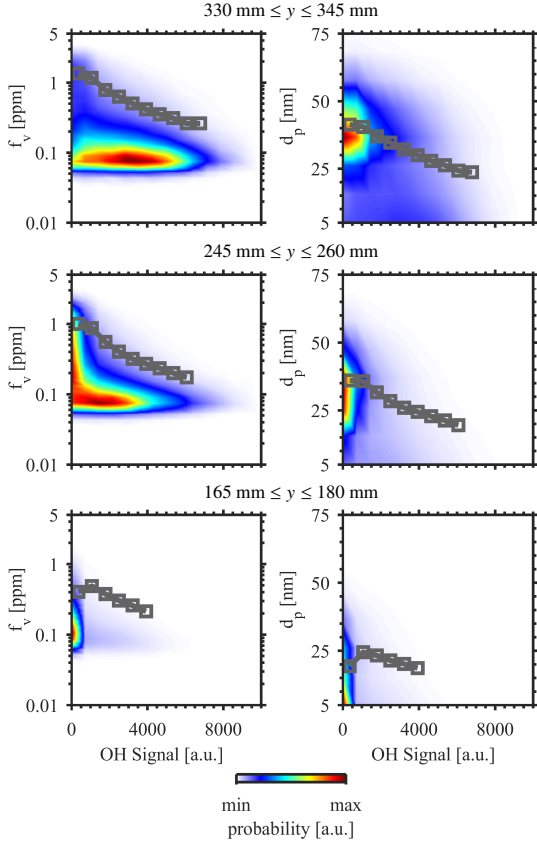

Figure 5: jpdfs of f_v and OH as well as d_p and OH at three locations. The gray line represents the mean of f_v and d_p conditioned on OH signal.

growth of particles due to condensation and surface reactions. In areas of low OH signal, f_v fluctuates by more than an order of magnitude from values below 0.1 ppm

to above 1 ppm, and d_p ranges from the detection limit up to diameters of approximately 60 nm. It is worth noting that the mean of f_v conditioned on OH does not coincide with the most probable value [29]. This is a characteristic feature of highly intermittent fields. The probability of soot and OH overlap is also significantly increased compared to the soot formation zone. Due to soot oxidation in the OH layer, the mean f_v and d_p conditioned on the OH gradually decrease as the OH signal increases. In the soot oxidation region, the probability of high f_v is considerably reduced compared to the mixing dominated zone. Meanwhile, the pdf of d_p indicates the presence of significantly larger primary particles at low OH signal intensities. Compared to the mixing dominated region, the conditional mean of f_v and d_p increases further at low OH signals, hence upstream of the reaction zone. Moreover, the jpdf of d_p and OH demonstrates that in addition to small particles, soot particles of significant diameter as large as $d_p \geq 35$ nm are present in the OH layer.

The simultaneously detected local gas temperature provides further information regarding the local interaction of soot and flame. As indium is oxidized under high temperatures and the presence of oxygen, the nTLAF measurements yield the temperature on the fuel rich side. The mean values of f_v and d_p conditioned on temperature and OH signal intensity in the soot oxidation region are shown in Fig. 6.

Although the mean f_v and d_p are reduced at axial locations $y \geq 315$ mm as shown in Fig. 2, the conditional mean values of f_v and d_p indicate the existence of soot clusters with high f_v and d_p at rather low temperatures and low OH signal intensity. Considering that nTLAF yields the temperature on the fuel rich side, the accumulation of soot occurs on the fuel rich side of the OH
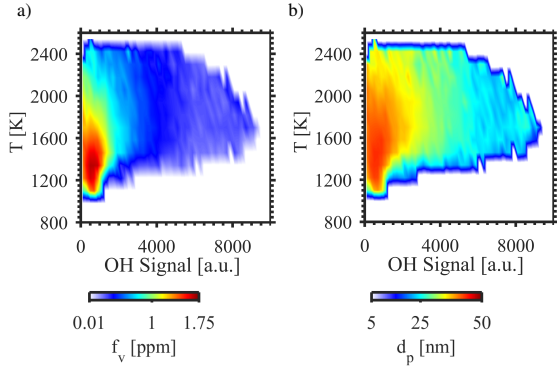
Figure 6: Mean of f_v (a) and d_p (b) conditioned on T and OH in the soot oxidation region (330 mm $\leq y \leq$ 345 mm).
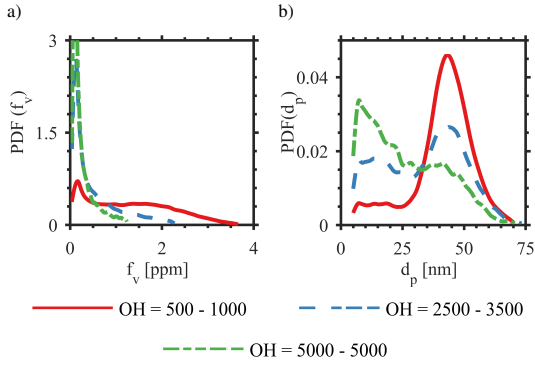

Figure 7: pdfs of f_v (a) and d_p (b) conditioned on OH signal obtained at 330 mm $\leq y \leq$ 345 mm.

layer. The same characteristic has been observed by Attili et al. [7], where it was shown that soot accumulates on the fuel rich side due to the preferential diffusion of soot [7].

Figure 6 reveals that the overlap of OH and soot occurs in a temperature range of 1500 and 2200 K, where f_v and d_p gradually decreases with increasing OH signal intensity due to soot oxidation. The conditional mean of d_p indicates the appearance of relatively large soot primary particles at high values of the OH signal. This finding and the pockets of soot on the lean side of the OH layer in Fig. 4 suggest that the soot oxidation rate is not sufficient to completely burn the soot transported by turbulent fluctuations through the flame. Different to the DNS by Attili et al. [7], where soot only emerged through locally extinguished flame patches, the soot might cross the OH layer before being completely oxidized.

To analyze the distribution of f_v and d_p on the fuel rich side and inside the OH layer, Fig. 7 presents the pdfs of f_v and d_p conditioned on three different OH sig-

nal ranges. As the overlap of soot and OH increases, the reduction of soot is apparent in the pdfs of f_v (Fig. 7a). With increasing OH signal, the distribution of f_v narrows and a distinct peak is obtained at low f_v. The distribution of d_p in Fig. 7b demonstrates that mostly particles with larger d_p are present on the fuel rich side of the OH layer, where OH concentration is small. With increasing soot–OH overlap, a bimodal distribution of d_p is observed, where the occurrence of large d_p decreases and more small primary particles are present. With increasing OH signal, the soot oxidation shifts the peak ratio towards small primary particles. Considering the slow reduction of larger primary particles, the rate for soot oxidation might be also rather slow. Noteworthy is, that this observation is vastly different to the typically used models which assume that soot is rapidly oxidized with the abundance of OH and O_2 [7].

5. Conclusions

Simultaneous, laser-based measurements of f_v, d_p, T, and OH have been performed in a turbulent pre-vaporized N_2–toluene non-premixed flame with a jet Reynolds number of 10000 and $Z_{st} = 0.23$ at various axial positions. The soot-flame interaction has been quantitatively analyzed in the three characteristic regions of the soot formation and oxidation process. In the turbulent flame, soot is formed at locations of high temperature in the absence of OH on the fuel side which is in good agreement with one-dimensional flamelet simulations. With increasing distance from the burner, f_v and d_p are increased due to soot growth and soot is present in a wide temperature range. Especially in the soot oxidation region, clusters of high f_v and d_p are present on the fuel rich side. The driving mechanism for the accumulation of the soot on the rich side is assumed to be the preferential diffusion of soot. It was found that the clusters of high f_v mostly consist of large primary particles. Inside the OH layer, a bimodal distribution of small and large d_p reveals a limited oxidation of soot particles. This finding and observations of soot clusters on the lean side of the OH layer suggest that soot is not completely oxidized in the OH layer.

References

[1] A. Seaton, D. Godden, W. MacNee, K. Donaldson, The Lancet 345 (8943) (1995) 176–178.

[2] M. Heal, P. Kumar, R. Harrison, Chem. Soc. Rev. 41 (19) (2012) 6606–6630.

[3] D. O. Lignell, J. H. Chen, P. J. Smith, Combust. Flame 155 (1) (2008) 316 – 333.

[4] H. Wang, Proc. Combust. Inst. 33 (1) (2011) 41 – 67.

[5] F. Bisetti, G. Blanquart, M. E. Mueller, H. Pitsch, Combust. Flame 159 (1) (2012) 317 – 335.

[6] A. Attili, F. Bisetti, M. E. Mueller, H. Pitsch, Combust. Flame 161 (7) (2014) 1849 – 1865.

[7] A. Attili, F. Bisetti, M. E. Mueller, H. Pitsch, Proc. Combust. Inst. 35 (2) (2015) 1215 – 1223.

[8] O. Park, R. A. Burns, O. R. Buxton, N. T. Clemens, Proc. Combust. Inst. 36 (1) (2017) 899 – 907.

[9] M. Köhler, K. P. Geigle, W. Meier, B. M. Crosland, K. A. Thomson, G. J. Smallwood, Appl. Phys. B 104 (2) (2011) 409–425.

[10] M. Köhler, K.-P. Geigle, T. Blacha, P. Gerlinger, W. Meier, Combust. Flame 159 (8) (2012) 2620 – 2635.

[11] D. Gu, Z. Sun, B. B. Dally, P. R. Medwell, Z. T. Alwahabi, G. J. Nathan, Combust. Flame 179 (2017) 33 – 50.

[12] S.-Y. Lee, S. R. Turns, R. J. Santoro, Combust. Flame 156 (12) (2009) 2264 – 2275.

[13] B. Franzelli, P. Scouflaire, S. Candel, Proc. Combust. Inst. 35 (2) (2015) 1921 – 1929.

[14] L. Cai, H. Pitsch, Combust. Flame 162 (5) (2015) 1623 – 1637.

[15] X. Liu, H. Wang, X. Wang, Z. Zheng, M. Yao, Appl. Energy 189 (2017) 187 – 200.

[16] S. Park, Y. Wang, S. H. Chung, S. M. Sarathy, Combust. Flame 178 (2017) 46 – 60.

[17] B. Choi, S. Choi, S. Chung, Proc. Combust. Inst. 33 (1) (2011) 609 – 616.

[18] P. R. Medwell, P. A. Kalt, B. B. Dally, Combust. Flame 148 (1) (2007) 48 – 61.

[19] J. Ye, P. R. Medwell, B. B. Dally, M. J. Evans, Combust. Flame 171 (2016) 173 – 184.

[20] K. K. Foo, Z. Sun, P. R. Medwell, Z. T. Alwahabi, B. B. Dally, G. J. Nathan, Combust. Flame 181 (2017) 270 – 282.

[21] P. R. Medwell, Q. N. Chan, P. A. M. Kalt, Z. T. Alwahabi, B. B. Dally, G. J. Nathan, Appl. Opt. 48 (6) (2009) 1237–1248.

[22] P. R. Medwell, Q. N. Chan, B. B. Dally, Z. T. Alwahabi, S. Mahmoud, G. F. Metha, G. J. Nathan, Appl. Phys. B 107 (3) (2012) 665–668.

[23] D. Gu, Z. Sun, G. J. Nathan, P. R. Medwell, Z. T. Alwahabi, B. B. Dally, Combust. Flame 167 (2016) 481 – 493.

[24] Z. Sun, D. Gu, G. Nathan, Z. Alwahabi, B. Dally, Proc. Combust. Inst. 35 (3) (2015) 3673 – 3680.

[25] Z. W. Sun, Z. T. Alwahabi, D. H. Gu, S. M. Mahmoud, G. J. Nathan, B. B. Dally, Appl. Phys. B 119 (4) (2015) 731–743.

[26] H. Pitsch, A c++ computer program for 0d combustion and 1d laminar flame calculations, Tech. rep., RWTH Aachen University (1998).

[27] A. Attili, F. Bisetti, M. E. Mueller, H. Pitsch, Combust. Flame 166 (2016) 192 – 202.

[28] S. R. Turns, F. H. Myhr, Combust. Flame 87 (3) (1991) 319 – 335.

[29] F. Bisetti, A. Attili, H. Pitsch, Phil. Trans. R. Soc. A 372 (2022) (2014) 20130324.